Carbon Resources Conversion 3 (2020) 112–121

Contents lists available at ScienceDirect

Carbon Resources Conversion

journal homepage: www.sciencedirect.com/journal/carbon-resources-conversion

Novel materials for solid oxide fuel cells cathodes and oxygen separation membranes: Fundamentals of oxygen transport and performance

Vladislav A. Sadykov [a,b,*], Ekaterina M. Sadovskaya [a,b], Nikita F. Eremeev [a], Elena Yu. Pikalova [c,d], Nina M. Bogdanovich [c], Elena A. Filonova [d], Tamara A. Krieger [a,b], Yulia E. Fedorova [a], Alexey V. Krasnov [a,b], Pavel I. Skriabin [a], Anton I. Lukashevich [a], Robert Steinberger-Wilckens [e], Izaak C. Vinke [f]

[a] Federal Research Center Boreskov Institute of Catalysis SB RAS, 630090 Novosibirsk, Russia
[b] Novosibirsk State University, 630090 Novosibirsk, Russia
[c] Institute of High Temperature Electrochemistry UB RAS, 620137 Yekaterinburg, Russia
[d] Ural Federal University, 620002 Yekaterinburg, Russia
[e] University of Birmingham, Edgbaston, Birmingham B15 2TT, UK
[f] Forschungszentrum Jülich GmbH, 52425 Jülich, Germany

ARTICLE INFO

Keywords:
Solid oxide fuel cells
Oxygen separation membranes
Oxygen mobility
Perovskites
Nanocomposites
Ruddlesden – Popper phases

ABSTRACT

In the field of modern hydrogen energy, obtaining pure hydrogen and syngas and then being able to use them for green energy production are significant problems. Developing solid oxide fuel cells (SOFC) and catalytic membranes for oxygen separation as well as materials for these devices is one of the most likely ways to solve these problems. In this work, the authors' recent studies in this field are reviewed; the fundamentals of developing materials for SOFC cathodes and oxygen separation membranes' permselective layers based on research of their oxygen mobility and surface reactivity are presented. Ruddlesden – Popper phases $Ln_{2-x}Ca_xNiO_{4+\delta}$ (LnCNO) and perovskite-fluorite nanocomposites $PrNi_{0.5}Co_{0.5}O_{3-\delta}$–$Ce_{0.9}Y_{0.1}O_{2-\delta}$ (PNC–YDC) were studied by isotope exchange of oxygen with $C^{18}O_2$ and $^{18}O_2$ in flow and closed reactors. For LnCNO a high oxygen mobility was shown ($D^* \sim 10^{-7}$ cm^2/s at 700 °C), being provided by the cooperative mechanism of oxygen migration involving both regular and highly-mobile interstitial oxygen. For PNC–YDC dominated a wide fast diffusion channel via fluorite phase and interphases due to features of the redistribution of cations resulting in superior oxygen mobility ($D^* \sim 10^{-8}$ cm^2/s at 700 °C). After optimization of composition and nanodomain structure of these materials, as cathodes of SOFC they provided a high power density, while for asymmetric supported oxygen separation membranes – a high oxygen permeability.

1. Introduction

Production of syngas and pure hydrogen is a key problem in the field of modern hydrogen energy. Another related problem is design of devices to produce energy from hydrogen, syngas and biofuels which are environmentally friendly. One branch linked to these problems relates to the design of solid oxide fuels cells (SOFC) and catalytic membrane reactors in general and materials for SOFC cathodes and oxygen separation membranes, or their permselective (functional) layers, in particular. Consequently, mixed ionic-electronic conductors (MIEC) need to be designed for these devices [1–7].

The key characteristics of the materials that affect the performance of these devices are related to oxygen mobility and surface reactivity (oxygen self-diffusion coefficient and surface exchange constant values) [4–9]. According to Adler – Lane – Steele model, the electrode performance correlates with the oxygen self-diffusion coefficient and surface exchange constant values of the material from which the electrode is

Abbreviations: EDX, energy-dispersive X-ray spectroscopy analysis; IIE, isothermal isotope exchange; LnCNO, $Ln_{2x}Ca_xNiO_{4+\delta}$; LSFC, $La_{1x}Sr_xFe_{1y}CoyO_{3\delta}$; LSFN, $La_{1x}Sr_xFe_{1y}NiyO_{3\delta}$; LSM, $La_{1x}Sr_xMnO_{3\delta}$; MF, GDC – $MnFe_2O_4$ – $Ce_{0.9}Gd_{0.1}O_{2\delta}$; MIEC, mixed ionic- electronic conductor; PNC, $PrNi_{0.5}Co_{0.5}O_{3\delta}$; PNC, YDC – $PrNi_{0.5}Co_{0.5}O_{3\delta}$ – $Ce_{0.9}Y_{0.1}O_{2\delta}$; RP, Ruddlesden – Popper phases; SOFC, solid oxide fuel cell; TEM, transmission electron microscopy; TPIE, temperature-programmed isotope exchange; XRD, X-ray diffraction; YDC, $Ce_{0.9}Y_{0.1}O_{2\delta}$.

* Corresponding author at: Federal Research Center Boreskov Institute of Catalysis SB RAS, 630090 Novosibirsk, Russia.
E-mail address: sadykov@catalysis.ru (V.A. Sadykov).

https://doi.org/10.1016/j.crcon.2020.08.002
Received 22 May 2020; Received in revised form 3 August 2020; Accepted 30 August 2020
Available online 11 September 2020

Nomenclature and units

a, b, c	unit cell parameters
E_D	effective activation energy of oxygen tracer diffusion coefficient
D^*	oxygen tracer diffusion coefficient
R_η	polarization resistance
δ	oxygen nonstoichiometry
1 W	1 $kg{\cdot}m^2{\cdot}s^{-3}$
1 Ω	1 $kg{\cdot}m^2{\cdot}s^{-3}{\cdot}A^{-2}$

fabricated as well as the microstructure features [6,8–10]. Moreover, the performance of a SOFC with a cathode fabricated from a material with high electronic but low oxide ionic conductivity is limited by triple phase boundary (gas phase – cathode – electrolyte). For a SOFC with MIEC cathode material the performance is limited by double phase boundary (gas phase – cathode) which improves the kinetics of the oxygen reduction reaction on cathode and oxide ions' transport to the electrolyte [1–7].

Oxygen separation membranes in catalytic reactors give the means to produce syngas as fuel for SOFCs. In such devices, biofuels (methane, ethanol, etc.) are oxidized by oxygen separated from air by a membrane. A promising approach to membrane design is that of an asymmetrical configuration with porous substrate and gas-tight permselective (functional) layer which has superior mechanical strength combined with higher oxygen fluxes [4–6]. It is essential that the materials for oxygen separation membranes (or their permselective layer in the case of asymmetrical configuration) possess a high mixed oxide-ionic and electronic conductivity in order to reach high oxygen fluxes across the membrane and to deliver superior performance in catalytic reactions (selective oxidation of fuels into syngas) [4–6].

The conventional materials used for SOFC cathodes and oxygen separation membranes are perovskites such as Sr-doped La manganites (LSM), ferrites-nickelates (LSFN) and ferrites-cobaltites (LSFC) [1–7]. Despite the high electronic (for LSM) or mixed ionic-electronic (for LSFN and LSFC) conductivity (~10^2–10^3 S/cm at 700 °C), these materials have issues concerning their thermomechanical and chemical compatibility with electrolyte materials (difference in thermal expansion coefficient and formation of poor conducting La and Sr zirconates/cerates at cathode-electrolyte interface) along with their low stability to carbonization which limits their application [1–7]. To abandon the strategy of doping the A-site with alkaline earth metal cations is one possible approach to improve the chemical stability of perovskite materials (such materials are more stable to carbonization) [5–7] as well as using host A-cations with smaller ionic radii (such as Pr^{3+} [9]) since their zirconates and cerates are thermodynamically unstable [1,2,6]. Pr nickelates-cobaltites (PNC) are promising materials for SOFC cathodes and permselective layers of oxygen separation membranes due to their compatibility with electrolytes (such as doped ceria), their stability to carbonization and their superior oxygen transport characteristics (oxygen tracer diffusion coefficient (D^*) value is up to ~ 10^{-8} cm^2/s at 700 °C) [4–6,12–15].

Another likely class of materials for these applications are Ruddlesden – Popper phases (RP) with regard to their moderate thermal expansion coefficients and a high mixed ionic-electronic conductivity [1–3,5–7,10,16–34]. The first homologues are A_2BO_4-like compounds, where A is La, Pr, Nd, etc. and B is Ni, Co, Cu, etc. RP phases demonstrate fine oxygen transport characteristics (D^* ~ 10^{-7} cm^2/s at 700 °C) due to the cooperative mechanism of oxygen migration involving both regular oxygen of perovskite layers ABO_3 and highly mobile interstitial oxygen of rock salt layers $A_2O_{2+\delta}$ [5–7,10,15,19,20,24–32].

In the current work, a review of the fundamentals of SOFC cathodes and the design of the oxygen separation membranes' materials based on investigations of their oxygen transport characteristics using isotope exchange of oxygen with $C^{18}O_2$ and $^{18}O_2$ in flow and closed reactors with detailed mathematical modeling for ground and powdered samples is presented. The authors' recent studies of perovskite-fluorite nanocomposites $PrNi_{0.5}Co_{0.5}O_{3-\delta}$–$Ce_{0.9}Y_{0.1}O_{2-\delta}$ (PNC–YDC) and Ruddlesden – Popper phases $Ln_{2-x}Ca_xNiO_{4+\delta}$ (LnCNO, Ln = La, x = 0 and 0.3; Ln = Pr, x = 0–0.6; Ln = Nd, x = 0–0.5) are reviewed. The results of testing symmetric cells' electrodes, SOFC cathodes and functional layers of asymmetric supported oxygen separation membranes are shown.

2. Materials and methods

$Ln_{2-x}Ca_xNiO_{4+\delta}$ (Ln = La, x = 0 and 0.3; Ln = Pr, x = 0–0.6; Ln = Nd, x = 0–0.5) were synthesized by a solution assisted solid state reaction [27,31], co-precipitation [28–30,32] and modified precursor (Pechini) techniques [5,30,33]. For the solid state reaction method, Ln_2O_3 (Ln = La, Pr and Nd), $Ca(NO_3)_2{\cdot}4H_2O$, $Ni(NO_3)_2{\cdot}6H_2O$ with a purity of no less than 99.5% (more information on starting materials is given in [27,29,31,34]) were used as starting materials in the respective stoichiometric ratios being mixed in a SAND planetary mill in isopropanol followed by drying and sintering at 1100 °C and then at 1150 °C with intermediate mechanical activation in the mill to obtain single-phase materials. The starting materials for co-precipitation and the Pechini methods as well as the synthesis procedures are described in [28,30,34] and [4,33], respectively.

$PrNi_{0.5}Co_{0.5}O_{3-\delta}$ and $Ce_{0.9}Y_{0.1}O_{2-\delta}$ were synthesized by a modified polymerized precursor (Pechini) method. Pr (III), Ni (II), Co (II), Ce (III) and Y (III) nitrates *n*-hydrates were used as starting materials being dissolved in water then mixed with citric acid – ethylene glycol solution followed by drying, firing and sintering at 700 °C as described in [12,13]. PNC – YDC nanocomposite was synthesized from initial PNC and YDC powders in weight ratio of 1:1 by ultrasonic dispersion in propanol-2 using a T25 (ULTRA-TURRAX IKA, Germany) homogenizer [12–14]. Final calcination temperature was chosen in the range of 1000–1250 °C depending on the composition.

All materials were characterized by X-ray diffraction (XRD) and transmission electron microscopy (TEM) with energy-dispersive X-ray spectroscopy (EDX) analysis [12–14,27–32]. XRD studies were performed using ARLX'TRA (Thermo, Switzerland), D8 Advance (Bruker, Germany), XRD-7000 (Shimadzu, Japan) diffractometers using Cu Kα monochromatic radiation in a 2θ range of 5–90°. The average scattering region size was determined using the Scherrer equation. The XRD patterns were analyzed by full-profile Rietveld refinement using Fullprof Suite software [35]. High resolution TEM micrographs were acquired using a JEM-2010 (Jeol, Japan) instrument with lattice resolution of 1.4 Å and acceleration voltage of 200 kV. EDX analysis was performed using a spectrometer with Si(Li) detector with energy resolution of 130 eV.

Oxygen transport characteristics were studied by the isotope heteroexchange of oxygen with $C^{18}O_2$ and $^{18}O_2$ in a closed reactor for powdered samples and in a flow reactor for ground samples (0.25–0.5 mm fraction). Temperature-programmed (TPIE) and isothermal (IIE) modes were used. For experiments in the closed reactor, a static installation was used with oxygen or carbon dioxide partial pressure of 1.4–2.1 Torr [4,13,27,33]. For the flow reactor experiments, samples were loaded in a quartz tube reactor with an inner diameter of 3 mm, then put into the gas flow. 1 % O_2 (or $^{18}O_2$) + He and 1 % CO_2 (or $C^{18}O_2$) + He gas mixtures were used at the flow rate of 25 ml/min. Gas phase composition was acquired by SRS QMS200 (for closed reactor experiments) and UGA-200 (for flow reactor experiments) mass spectrometers (Stanford Research Systems, USA). Mathematical modeling [5,6,27,36,37] and a nonnumeric method [38] were used to obtain the oxygen tracer diffusion coefficient (D^*) and surface exchange constant (k^*) from the TPIE and IIE data.

Symmetrical cells were fabricated using dense $Ce_{0.8}Sm_{0.2}O_{1.9}$ electrolyte substrates [27,34,39]. Electrode layers were deposited on the substrates as described elsewhere [39] followed by sintering at

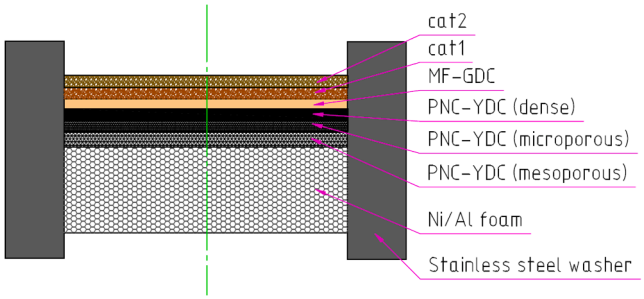

Fig. 1. Scheme of the asymmetric supported oxygen separation membrane.

1100–1300 °C. The thickness and porosity of the electrode layers were estimated to be ~ 25–28 μm and ~ 35–40%, respectively. The electrochemical characteristics were studied by electrochemical impedance performed using a FRA-1260 Frequency Response Analyzer with an EI-1287 electrochemical interface [27]. Tests were carried out in the temperature range of 550–850 °C in air atmosphere in the frequency range of 0.01 Hz to 100 kHz at an applied sinusoidal signal of 20–30 mV and fitted using ZView2 software.

Single button anode supported solid oxides fuel cells were prepared using anodic $Ce_{0.9}Y_{0.1}O_{2-\delta}|Ce_{0.9}Gd_{0.1}O_{2-\delta}|Ni/Zr_{0.84}Y_{0.16}O_{2-\delta}$ half-cells (2×2 cm^2 and 4×4 cm^2) as substrates [5,7,12,40]. Cathode layers were deposited on the substrate from inks prepared from the powders by painting and screen printing followed by sintering at 1100 °C. The thickness of cathodes obtained was ~ 20 μm. Voltammetric characteristics were obtained using humidified hydrogen as a fuel supplied to the anode with a flow rate of 100 ml/min and dry compressed air as an oxidant fed to the cathode with a flow rate of 200 ml/min [12,40]. For small cells Pt and Ni gauzes were used as current collectors. For full-size single cells testing was carried out using a layer of $La_{0.58}Sr_{0.4}MnO_{3-\delta}$ (thickness 60–70 μm) as cathode current collector and Pt gauze as anode current collector [40].

Asymmetric supported membranes (Fig. 1) for oxygen separation were fabricated using improved Ni/Al foam substrates with graded porosity. Mesoporous, microporous and dense PNC – YDC permselective layers, a dense $MnFe_2O_4$ – $Ce_{0.9}Gd_{0.1}O_{2-\delta}$ (MF – GDC) buffer layer, then $Pt/Sm_{0.15}Pr_{0.15}Ce_{0.35}Zr_{0.3}O_{2-\delta}$ (cat1) and $LaNi_{0.9}Pt_{0.1}O_3/Pr_{0.2}Ce_{0.4}Zr_{0.4}O_{2-\delta}/Al_2O_3$ (cat2) catalytic layers were deposited in sequence from suspensions by vacuum slip casting and then sintered at 1100 °C (or 900 °C for catalytic layers). The membranes were tested in methane selective oxidation into syngas and oxi-dry reforming using a purpose-built kinetic setup [5,14,41,42] and an oven-placed double-flange reactor assembly.

3. Calculations

Atomic isotope fraction of ^{18}O in O_2 or CO_2 (α) and molecular fraction of $^{16}O^{18}O$ or $C^{16}O^{18}O$ (f_{16-18}) in the gas phase were calculated as follows:

$$\alpha = \frac{I_{48} + 0.5 \times I_{46}}{I_{44} + I_{46} + I_{48}}, f_{16-18} = \frac{I_{46}}{I_{44} + I_{46} + I_{48}}, \quad (1)$$

where I_{44}, I_{46} and I_{48} are intensities of parent peaks at $m/z = 44$, 46 and 48, respectively. Responses of α and f_{16-18} were analyzed using a mathematical model [5,6,15,29,36,37]:

$$\frac{\partial \alpha_g}{\partial t} + O(\tau) = \frac{N_S}{N_g} R^{\Sigma}(\alpha_s - \alpha_g), \quad (2)$$

$$\frac{\partial \alpha_s}{\partial t} = R^{\Sigma}(\alpha_g - \alpha_s) - \frac{N_{bulk}}{N_s} \frac{D^*}{h^2} \left.\frac{\partial \alpha_{bulk}}{\partial \eta}\right|_{\eta=0}, \quad (3)$$

$$\frac{\partial \alpha_{bulk}}{\partial t} = \frac{D^*}{h^2} \frac{\partial^2 \alpha_{bulk}}{\partial \eta^2}, \quad (4)$$

$$\frac{\partial f_{16-18}}{\partial t} + O(\tau) = R^0(2\alpha_g(1-\alpha_g) - f_{16-18}) + \frac{N_S}{N_g}(R^2(2\alpha_s(1-\alpha_s) - f_{16-18}) + R^1(\alpha_g(1-\alpha_s) + \alpha_s(1-\alpha_g) - f_{16-18})). \quad (5)$$

The initial and boundary conditions were: $t = 0 \Rightarrow \alpha_i = \alpha_i^o$.

In Eqs. (2)–(5), α_g, α_s and α_{bulk} designate ^{18}O atomic fractions in the gas phase, on the samples' surface and in the samples' bulk, respectively; N_g, N_s and N_{bulk} are amounts of oxygen atoms in the gas phase, oxide anions on the samples' surface and in the samples' bulk, respectively; f_{16-18} is the $^{16}O^{18}O$ or $C^{16}O^{18}O$ molecular fraction in the gas phase; R^0, R^1, R^2 are the rates of exchange going by different types of mechanism according to the Muzykantov classification [6,7,36,43–45]; $R^{\Sigma} = 0.5R^1 + R^2 = k^* N_{bulk}/V_{sample}$ is the total heteroexchange rate, k^* is the oxygen surface exchange constant, V_{sample} is the total volume of sample; D^* is the oxygen tracer diffusion coefficient; h is the characteristic particle size of the sample, η is the dimensionless parameter of the distance from the particle surface; t is time; $O(\tau)$ is an operator depending on the mass transport mode in the reactor:

$$O(\tau) = \begin{cases} 0 & \text{- for closed reactor} \\ \frac{1}{\tau} \frac{\partial \alpha_g(or f_{16-18})}{\partial \xi} & \text{- for flow reactor} \end{cases} \quad (5)$$

where τ is the contact time in the reactor, ξ is the dimensionless sample length. The rates of exchange and oxygen tracer diffusion coefficients are considered to obey the Arrhenius law:

$$R^{(i)} = R^{(i)}_{ref} \exp\left(-\frac{E_{R(i)}}{RT'}\right), D^* = D^*_{ref} \exp\left(-\frac{E_D}{RT'}\right), T' = \frac{T\,T_{ref}}{T_{ref} - T}, \quad (6)$$

where $R^{(i)}_{ref}$ and D^*_{ref} are the exchange rate and tracer diffusion coefficient at the reference temperature T_{ref}; $E_{R(i)}$ and E_D are their effective (apparent) activation energies [5,6,36,37].

IIE data were also analyzed using a nonnumeric method suggested in the works [38,46]. The heteroexchange rate is associated with a jump value of ^{18}O atomic fraction outlet after the isotopic switch (α_τ):

$$\alpha_\tau = \alpha^{input} exp(-bR^{\Sigma}\tau), \quad (7)$$

Table 1
Crystal structure and oxygen over-stoichiometry of the $Ln_{2-x}Ca_xNiO_{4+\delta}$ materials [15,27–32].

Sample	$La_{2-x}Ca_xNiO_{4+\delta}$		$Pr_{2-x}Ca_xNiO_{4+\delta}$			$Nd_{2-x}Ca_xNiO_{4+\delta}$		
x	0.0	0.3	0.0	0.3	0.5	0.0	0.3	0.5
Structure	O	T	O	T	O	O	T	O
Sp. gr.	*Fmmm*	*I4/mmm*	*Fmmm*	*I4/mmm*	*Bmab*	*Fmmm*	*I4/mmm*	*Bmab*
a, [Å]	5.4629	3.8288	5.3923	3.8044	5.3373	5.3759	3.7993	5.3076
b, [Å]	5.4664	3.8288	5.4610	3.8044	5.3590	5.4596	3.7993	5.3625
c, [Å]	12.6828	12.5984	12.4441	12.3900	12.3590	12.3652	12.2928	12.2772
χ^2	4.99	6.09	10.7	7.18	6.65	6.14	6.85	8.52
PDF#	81–2413	79–9864	89–0130	58–0852	78–2196	83–9908	75–2834	79–1092
δ (25 °C)	0.13	0.06	0.25	0.09	0.01	0.20	0.11	0.04

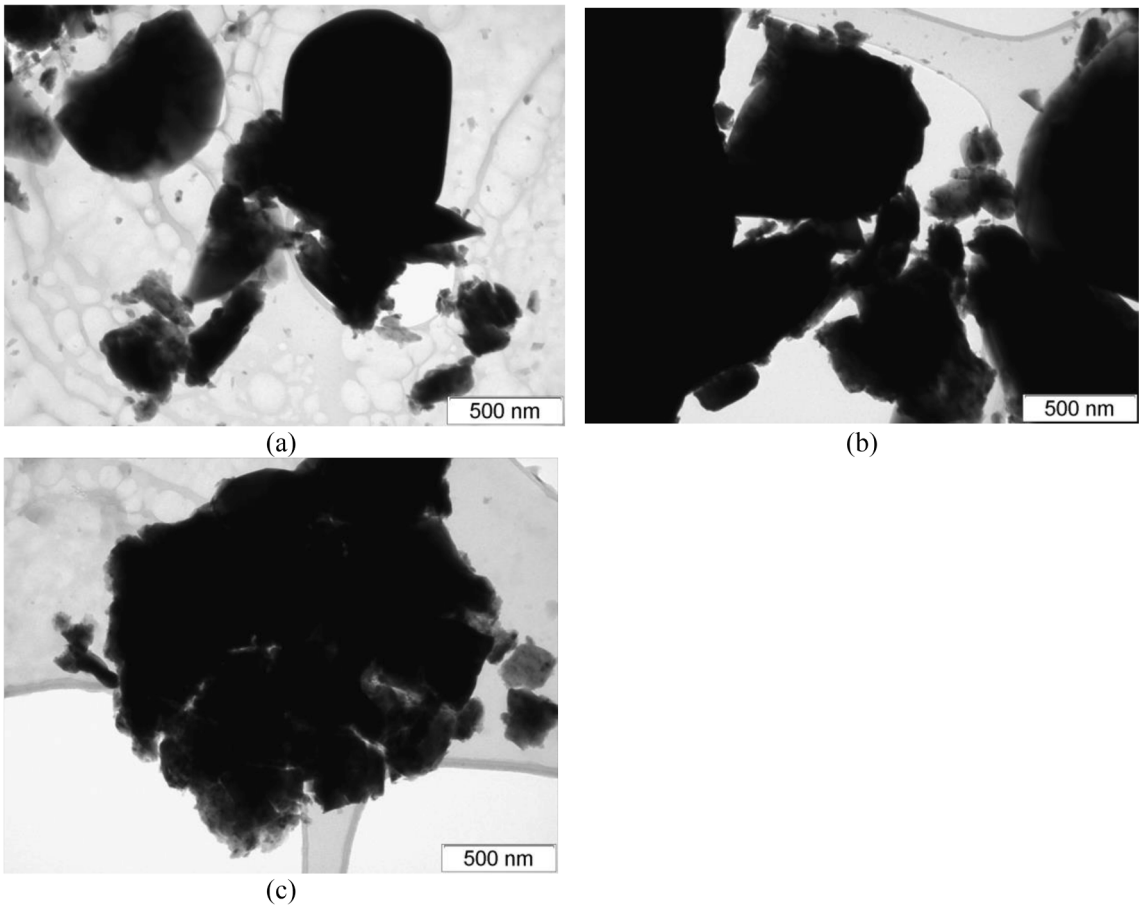

Fig. 2. TEM micrographs of $Ln_{1.7}Ca_{0.3}NiO_{4+\delta}$: Ln = La (a), Pr (b) and Nd (c).

where $b = N_{bulk}/N_g$ describes the ratio of exchangeable oxide oxygen to the number of oxygen atoms in the gas phase. Time dependence of average values of ^{18}O fraction on the surface over the reactor length and average isotope fraction in the oxide bulk can be calculated as:

$$\alpha_s(t) = \frac{\alpha(t) - \alpha^{input} exp(-\tau bR)}{1 - exp(-\tau bR)} = \frac{\alpha(t) - \alpha_\tau}{1 - \alpha_\tau/\alpha^{input}}, \quad (8)$$

$$\alpha_{bulk}(t) = \frac{1}{\tau b}\int_0^t (\alpha^{input} - \alpha(t))dt. \quad (9)$$

Oxygen tracer diffusion coefficient value can be estimated according to the equation:

$$\frac{D^*}{h^2} = \frac{1}{2.3}\lim_{t\to\infty}\left[\frac{\alpha^{input} - \alpha(t,1)}{\tau b\tilde{\alpha}_s(t) - \int_0^t(\alpha^{input} - \alpha)dt.}\right] \quad (10)$$

4. Results and discussion

4.1. Structure features

According to the XRD data, LnCNO materials were single phase oxides with orthorhombic (O) or tetragonal (T) Ruddlesden – Popper structure (Table 1). The space group was *Fmmm*, *I4/mmm* or *Bmab* depending on Ca content. At low doping levels, O – T phase transition while increasing × in $Ln_{2-x}Ca_xNiO_{4+\delta}$ is related to lowering the interstitial oxygen content due to charge compensation. At a higher Ca content, T – O phase transition might probably be explained by the Jahn – Teller Ni^{3+} cations' content increasing [15,27–32]. Structure details and δ values are summarized in Table 1. According to TEM data [27,28,31,32], very large (characteristic size ~ 0.5–1 μm) particles were observed, which can be attributed to the high sintering temperatures (1100–1250 °C). Examples of TEM images are given in Fig. 2. Extended defects (cluster inclusions, grain boundaries and stacking faults) were

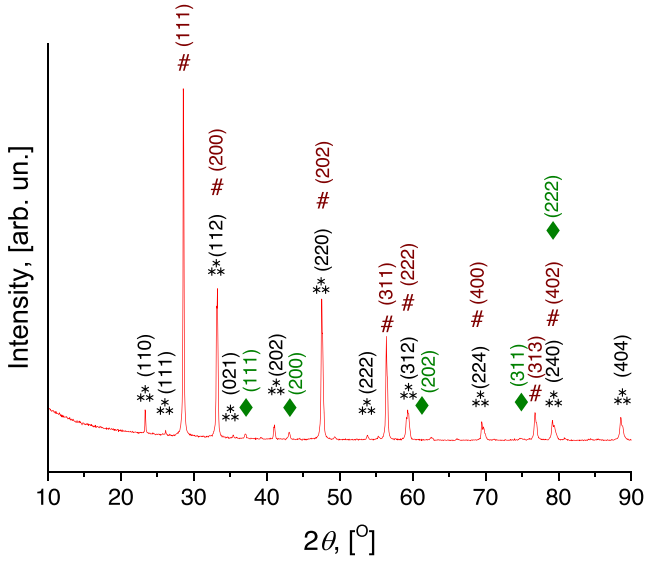

Fig. 3. XRD pattern of $PrNi_{0.5}Co_{0.5}O_{3-\delta}$ – $Ce_{0.9}Y_{0.1}O_{2-\delta}$ nanocomposite. ⁂ – perovskite phase with average composition of $Pr_{0.8}Ni_{0.5}Co_{0.5}O_{3-\delta}$ (PDF#66–0348), # - fluorite phase with average composition of $Ce_{0.65}Pr_{0.25}Y_{0.1}O_{2-\delta}$ (PDF#75–0174), ◆ – NiO (PDF#75–0269). (*hkl*) indices: black – perovskite, wine – fluorite, green – NiO [12–15].

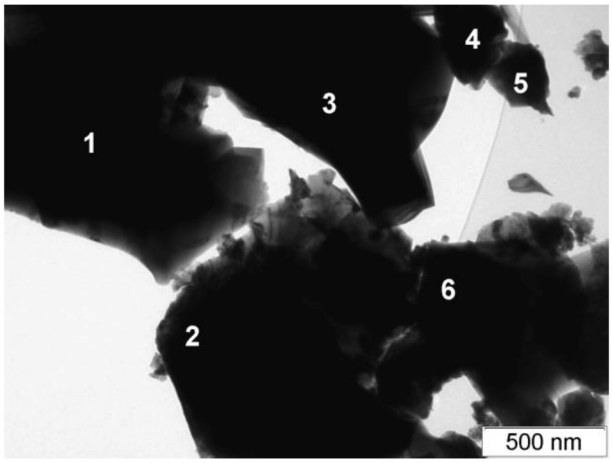

(a)

Atomic % by Element

	Y L	CeL	PrL	CoK	NiK
1	1.06	6.12	69.13	13.44	10.24
2	4.69	48.06	43.23	2.12	1.9
3	1.2	11.07	45.1	16.32	26.31
4	1.92	33.26	61.8	1.89	1.12
5	1.01	3.93	68.83	14.9	11.33
6	1.09	6.51	3.18	30.01	59.21

(b)

Fig. 4. High-resolution TEM micrograph (a) and EDX analysis for $PrNi_{0.5}Co_{0.5}O_{3-\delta}$ – $Ce_{0.9}Y_{0.1}O_{2-\delta}$.

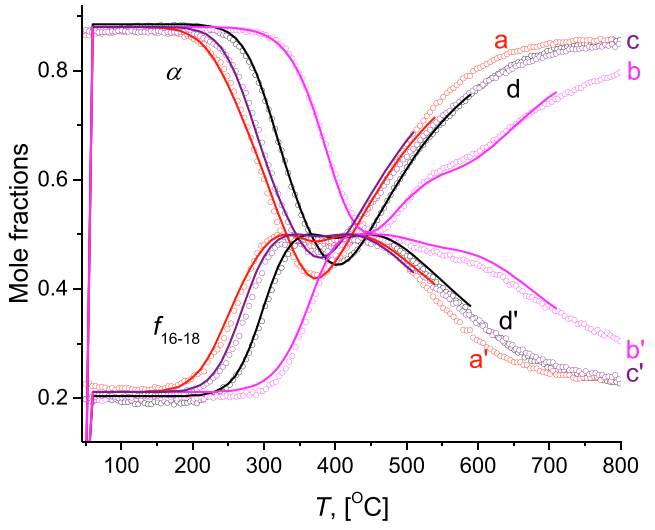

Fig. 5. Temperature-programmed isotope exchange of oxygen with $C^{18}O_2$ in the flow reactor: (a,a') $La_2NiO_{4+\delta}$, (b,b') $La_{1.7}Ca_{0.3}NiO_{4+\delta}$, (c,c') $Pr_2NiO_{4+\delta}$, (b, b') $Pr_{1.7}Ca_{0.3}NiO_{4+\delta}$.

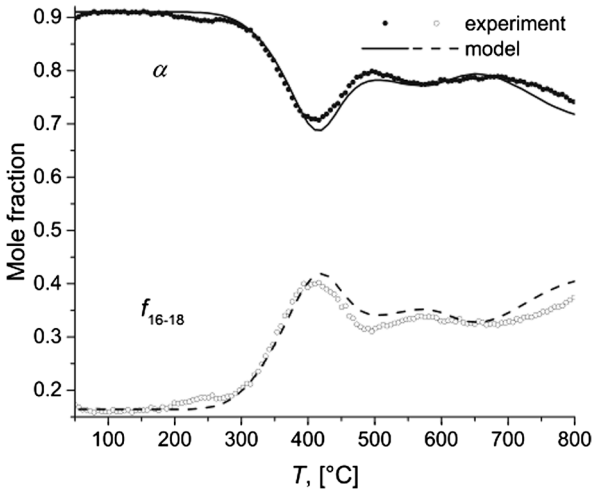

Fig. 6. Temperature programmed isotope exchange of oxygen with $C^{18}O_2$ in the flow reactor for the $Pr_{1.4}Ca_{0.6}NiO_{4+\delta}$ sample [15,28].

observed. Amorphous nanoparticles, probably consisting of CaO, NiO or (Ca,Ni)O, were present in some samples.

The XRD pattern of the PNC – YDC nanocomposite sintered at 1100 °C is given in Fig. 3. The unit cell parameters are $a = 5.3750$ Å, $b = 7.6040$ Å, $c = 5.3960$ Å for the perovskite phase and $a = 5.4030$ Å for the fluorite phase. The average X-ray particle size is > 100 nm, which is in agreement with the TEM data. According to the XRD and EDX data (Fig. 4), redistribution of cations between phases takes place: Pr^{3+} cations migrate from the PNC phase to the doped ceria phase incorporating into the latter. Depletion of the perovskite phase by cations probably leads to the formation of local cation deficiency and structure disordering [12]. Obviously, this causes disordering of the fluorite phase as well. For different domains of the fluorite phase, the Pr/Ce ratio varies from 0 to 1 according to the TEM with EDX analysis which shows that the composition of the domains is controlled by kinetics (cation diffusion) and not by equilibrium [13]. The average compositions of the perovskite and fluorite phases according to the TEM with EDX analysis are $Pr_{0.8}Ni_{0.5}Co_{0.5}O_{3-\delta}$ and $Ce_{0.65}Pr_{0.25}Y_{0.1}O_{2-\delta}$ [4–6,12–15].

4.2. Oxygen mobility and surface reactivity

For the undoped $Ln_2NiO_{4+\delta}$ (Ln = La, Pr, Nd) samples the process of isotope substitution starts at $T \sim 200$ °C for exchange with $C^{18}O_2$ and at $T \sim 500$ °C for exchange with $^{18}O_2$ and involves almost 100 % of the bulk oxygen during the TPIE run indicating high oxygen mobility. Doping with Ca shifts this temperature upward (Fig. 5). Further increase of Ca content leads to the appearance of 2–3 peaks in the TPIE with $C^{18}O_2$ curves (Fig. 6) showing nonuniformity of the bulk oxygen diffusivity for Ln = La, Pr, while the curve shape with a single peak is preserved across the entire $Nd_{2-x}Ca_xNiO_{4+\delta}$ series in the range of × = 0–0.5 [27–32].

According to modeling of the TPIE with $C^{18}O_2$ data, the bulk diffusion is a limiting process, so the surface exchange constant values cannot be estimated in many cases. Typical k^* values acquired from the TPIE with $^{18}O_2$ data are ~ 10^{-7}–10^{-6} cm/s at 700 °C [27–32].

For undoped $Ln_2NiO_{4+\delta}$ and RP phases with a low Ca content typical D^* values are ~ 10^{-7} cm^2/s at 700 °C. The effective activation energy (E_D) values vary within the range of 80–140 kJ/mole depending on the host A cation nature and dopant content. Such a high level of oxygen mobility is caused by the cooperative mechanism of its migration [5–7,10,15,19,20,24–32,47–51]. This mechanism involves the lattice oxygen of perovskite layers and the highly mobile interstitial oxygen of

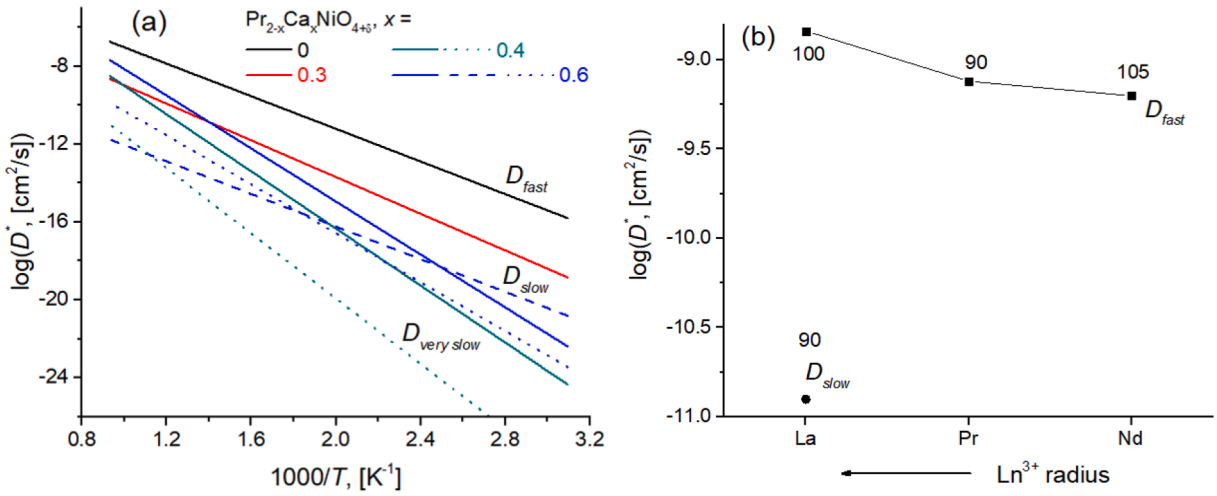

Fig. 7. (a) Arrhenius plots of the oxygen tracer diffusion coefficient for $Pr_{2-x}Ca_xNiO_{4+\delta}$ according to the modeling of the TPIE with $C^{18}O_2$ data [15,28]. (b) Oxygen tracer diffusion coefficients at 700 °C depending on Ln nature for $Ln_{1.7}Ca_{0.3}NiO_{4+\delta}$; labels are the effective activation energy values, [kJ/mole] [6,15,27–32].

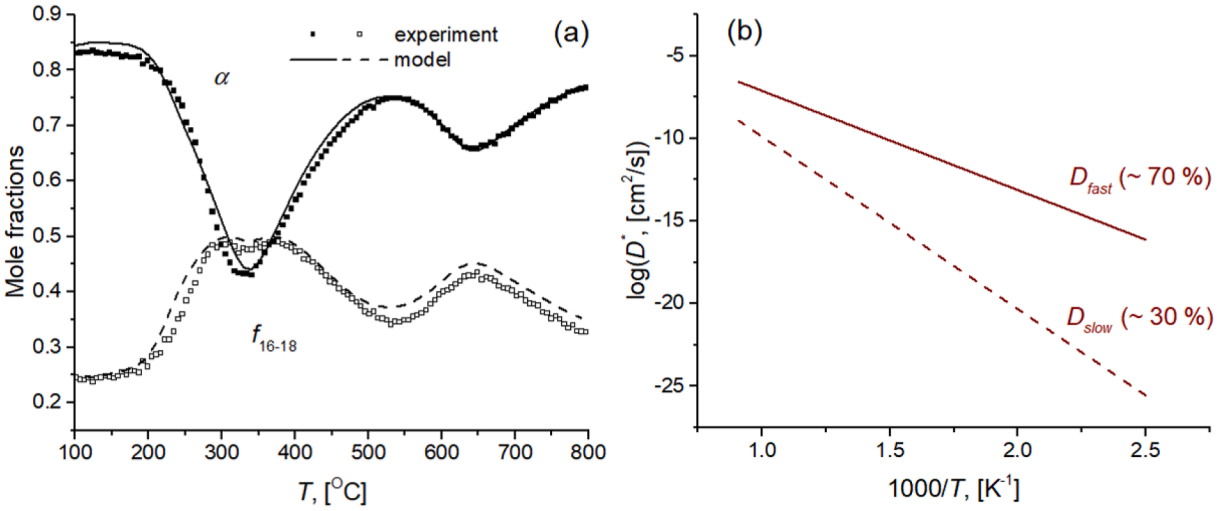

Fig. 8. Temperature-programmed isotope oxygen exchange with $C^{18}O_2$ in the flow reactor (a) and Arrhenius plots for oxygen tracer diffusion coefficient (D^*) (b) for PNC – YDC [6,12–15].

rock salt layers with the latter being able to accumulate in a large amount (Table 1). The interstitial oxide anion moves through the $Ln_{3-x}Ca_x$ triangle displacing the oxide anion located in the apical position of the NiO_6 octahedra. Then the apical oxide anion passes through the neighboring $Ln_{3-x}Ca_x$ triangle to be located in the near interstitial position. This process is also accompanied by the cooperative motion of polyhedra. Oxygen vacancies in apical sites of perovskite layers can also be involved in the migration mechanism [47,49–51]. These vacancies can also migrate between various positions and even jump into the neighboring perovskite layer.

Increasing Ca content in $Ln_{2-x}Ca_xNiO_{4+\delta}$ results in nonuniformity of the bulk oxygen diffusivity. This phenomenon was observed at $\times = 0.3$ for Ln = La, $x \geq 0.4$ for Ln = Pr and was not observed at $0 \leq x \leq 0.5$ for Ln = Nd [6,15,27–32]. 1–2 additional channels of slow oxygen diffusion appear. As mentioned above, these channels were observed as additional peaks in the TPIE with $C^{18}O_2$ curves. Examples of TPIE curves with 3 peaks corresponding to 'fast', 'slow' and 'very slow' diffusion channels are shown in Fig. 6. D^* values acquired from the TPIE data for the samples with different Ca content and host cations are compared in Fig. 7.

Such a decrease in overall oxygen mobility can be caused by the cooperative mechanism of oxygen migration being hampered [27–32]. The first probable reason is associated with the highly-mobile interstitial oxygen content decreasing as a result of charge compensation as Ln^{3+} cations are replaced by Ca^{2+} cations. The second reason appears to be steric hindrances for anions while passing through $Ln_{3-x}Ca_x$ triangles since Ca^{2+} cations have a larger ionic radius [11] which leads to an increased energy barrier for oxide anions hops between the interstitial and apical oxygen positions [27–29].

The TPIE with $C^{18}O_2$ curves acquired for the PNC – YDC nanocomposite are shown in Fig. 8(a). The exchange process starts at $T \sim 200$ °C and involves 80 % of the overall nanocomposite bulk oxygen during the TPIE run which demonstrates a high oxygen mobility. Two peaks in the TPIE curves are clearly distinguished showing nonuniformity of the bulk oxygen [12–14].

According to the TPIE data modeling, diffusion is a limiting stage, so the k^* values cannot be estimated from the data obtained. Two channels of oxygen diffusion were revealed. The fast one corresponding to a low/intermediate-temperature peak is related to the perovskite-fluorite interfaces and the fluorite phase, while the slow one corresponding to a high-temperature peak is related to the perovskite phase [12–14]. This is revealed by the comparison with the oxygen mobility of the individual phases of the respective compositions which the nanocomposite consists of (Section 4.1) [14,52,53]. The oxygen tracer diffusion coefficient

Table 2
Oxygen tracer diffusion coefficient (D^*) and surface exchange constant (k^*) values for state-of-the-art materials of solid oxide fuel cell cathodes and oxygen separation membranes [4,6,7,10,12–14,28,29,48,59–61].

Composition	Method*	T, [°C]	D^*, [cm^2/s]	k^*, [cm/s]	Reference
$La_{0.7}Sr_{0.3}MnO_{3\pm\delta}$	IIE $^{18}O_2$	900	$>9\cdot10^{-12}$	$>3.9\cdot10^{-7}$	[7,59]
$La_{0.8}Sr_{0.2}Fe_{0.7}Ni_{0.3}O_{3-\delta}$	IIE $^{18}O_2$	700	$>6\cdot10^{-14}$	–	[7]
$La_{0.8}Sr_{0.2}Fe_{0.7}Ni_{0.3}O_{3-\delta}$ – $Ce_{0.9}Gd_{0.1}O_{2-\delta}$	IIE $^{18}O_2$	700	$\geq9\cdot10^{-14}$ (perovskite) $3\cdot10^{-13}$ (fluorite) $\geq5\cdot10^{-8}$ (interface)	$3.6\cdot10^{-8}$	[4,7]
$PrNi_{0.5}Co_{0.5}O_{3-\delta}$ – $Ce_{0.9}Y_{0.1}O_{2-\delta}$	TPIE $C^{18}O_2$	700	$4.9\cdot10^{-8}$ (fast) $6.1\cdot10^{-11}$ (slow)	–	[6,12–14]
$La_2NiO_{4+\delta}$	TPIE $C^{18}O_2$	700	$5.5\cdot10^{-10}$	$7.7\cdot10^{-5}$	[6,29]
$La_2NiO_{4+\delta}$	IEDP SIMS	700	$4.8\cdot10^{-8}$	$2.1\cdot10^{-6}$	[10,48]
$La_{1.7}Ca_{0.3}NiO_{4+\delta}$	TPIE $C^{18}O_2$	700	$1.5\cdot10^{-9}$ (fast) $1.3\cdot10^{-11}$ (slow)	$6.0\cdot10^{-6}$	[6,29]
$Pr_2NiO_{4+\delta}$	TPIE $C^{18}O_2$	700	$7.0\cdot10^{-8}$	$9.5\cdot10^{-5}$	[6,28]
$Pr_2NiO_{4+\delta}$	IEDP SIMS	700	$7.2\cdot10^{-8}$	$1.4\cdot10^{-6}$	[10,48]
$Pr_{1.7}Ca_{0.3}NiO_{4+\delta}$	TPIE $C^{18}O_2$	700	$7.6\cdot10^{-10}$	$2.4\cdot10^{-4}$	[6,28]
$Pr_{1.5}Ca_{0.5}NiO_{4+\delta}$	TPIE $C^{18}O_2$	700	$\sim5\cdot10^{-9}$ (fast) $4.0\cdot10^{-11}$ (slow) $2.4\cdot10^{-13}$ (very slow)	$8.9\cdot10^{-7}$	[6,28]
$Nd_2NiO_{4+\delta}$	TPIE $C^{18}O_2$	700	$4.5\cdot10^{-8}$	–	[6,29,31]
	TPIE $^{18}O_2$	700	–	$5.9\cdot10^{-8}$	
$Nd_2NiO_{4+\delta}$	IEDP SIMS	700	$4.5\cdot10^{-8}$	$3.4\cdot10^{-7}$	[10,48]
$Nd_{1.8}Ca_{0.2}NiO_{4+\delta}$	IEDP SIMS	700	$1.0\cdot10^{-8}$	$1.9\cdot10^{-7}$	[10,48]
$Nd_{1.7}Ca_{0.3}NiO_{4+\delta}$	TPIE $C^{18}O_2$	700	$6.2\cdot10^{-10}$	–	[6,29,31]
	TPIE $^{18}O_2$	700	–	$8.3\cdot10^{-8}$	
$PrBaCo_2O_{5+\delta}$	IEDP SIMS	670	$2\cdot10^{-8}$	$8\cdot10^{-7}$	[60]
$PrBaCo_2O_{5+\delta}$	ECR	400	$1\cdot10^{-7}$	$2\cdot10^{-5}$	[61]
	IEDP SIMS	400	$1\cdot10^{-7}$	$2\cdot10^{-6}$	

* IEDP SIMS – isotope exchange depth profiling with secondary-ions mass-spectrometry, ECR – electric conductivity relaxation.

values calculated from the TPIE data are ~ 10^{-8} cm^2/s and ~ 10^{-10} cm^2/s at 700 °C for fast and slow diffusion channels, respectively (Fig. 8(b)).

Hence, fine oxygen transport properties were shown for the PNC – YDC nanocomposite. The fast diffusion channel within the fluorite phase and along the perovskite- fluorite interfaces dominates, involving ~ 70 % of the bulk oxygen. These transport features are caused by the structural properties, the cations' redistribution and also the developed perovskite-fluorite interfaces [4–7,12–15,52,53]. As mentioned above, Pr cations partially leave the perovskite phase and are incorporated into the fluorite phase. In Pr- and Y-doped ceria, Pr cations can easily vary their charge 3+/4 + resulting in forming ordered $Pr^{3+/4+}$ chains providing a high oxygen mobility of the fluorite phase [54,55]. This, and the other well-known feature of nanocomposites related to developed interfaces, are responsible for the excellent oxygen transport properties of the PNC – YDC nanocomposite [4–6,12–15].

The comparison of oxygen mobility of the materials reviewed in this work and other state-of-the-art materials for solid oxide fuel cell cathodes and oxygen separation membranes is given in Table 2. Hence, according to the isotope exchange studies, RP phases and PNC – YDC demonstrate a high oxygen mobility and surface reactivity. Such characteristics derive from the cooperative mechanism of oxygen migration for the former and by the cations' redistribution features for the latter. Despite the negative effects of doping with Ca on the oxygen mobility of RP phases, it remains rather high even for the samples with a high dopant content. Ionic and ambipolar conductivity values estimated by Nernst – Einstein law [56] are ~ 10^{-3}–10^{-1} S/cm at 700 °C [27–32] which is close to those for doped ceria electrolytes [5,56–58] and are high enough to obtain high oxygen fluxes in oxygen separation membranes. High D^* and k^* values ensure excellent electrode performance as predicted by the Adler – Lane – Steel model [8–10,29,32]. A high oxygen mobility should also provide a high O_2 flux across the oxygen separation membrane which is required for good performance in catalytic reactions of fuel oxidation by oxygen separated from air [4–6].

4.3. Performance of symmetric cells and solid oxide fuel cells

Electrical impedance studies carried out for the symmetrical cells

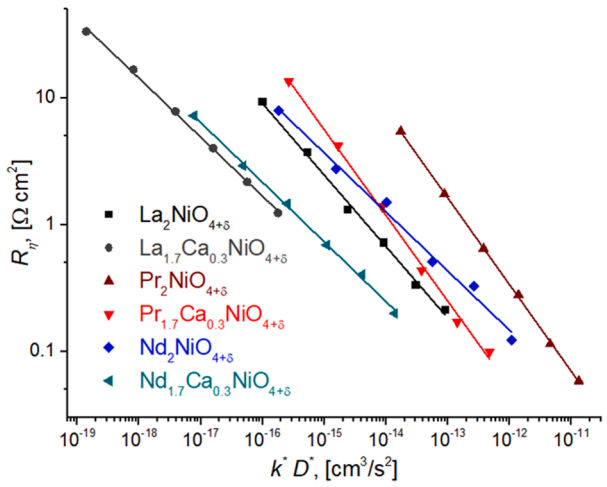

Fig. 9. Correlation between polarization resistance (R_η) and oxygen transport characteristics [13,25–30].

with LnCNO electrode layers have demonstrated the effect of doping with Ca revealing itself differently depending on the nature of the Ln cation [14,26–31,33,38]. However, no direct interrelation of the electrode activity with either the electrical properties or the interstitial oxygen content was shown in all cases. For the $La_{2-x}Ca_xNiO_{4+\delta}$-based electrodes, doping with Ca significantly increased the polarization resistance of the electrodes (R_η = 0.73 Ω cm^2 and 4.01 Ω cm^2 at 700 °C for × = 0.0 and 0.3, respectively), while total conductivity increased (σ_{total} = 58 S/cm and 93 S/cm at 700 °C for × = 0.0 and 0.3, respectively). For the $Pr_{2-x}Ca_xNiO_{4+\delta}$-based electrodes, the lowest R_η values were obtained at × = 0.1 (0.17 Ω cm^2) while the highest total conductivity was reached at × = 0.5 (145 S/cm). For the $Nd_{2-x}Ca_xNiO_{4+\delta}$-based electrodes, the lowest polarization resistance was obtained for the sample with × = 0.4 (0.37 Ω cm^2), at the same time the highest conductivity was reached at × = 0.3 (133 S/cm) [26–31].

However, correlation of the polarization resistance of the electrodes

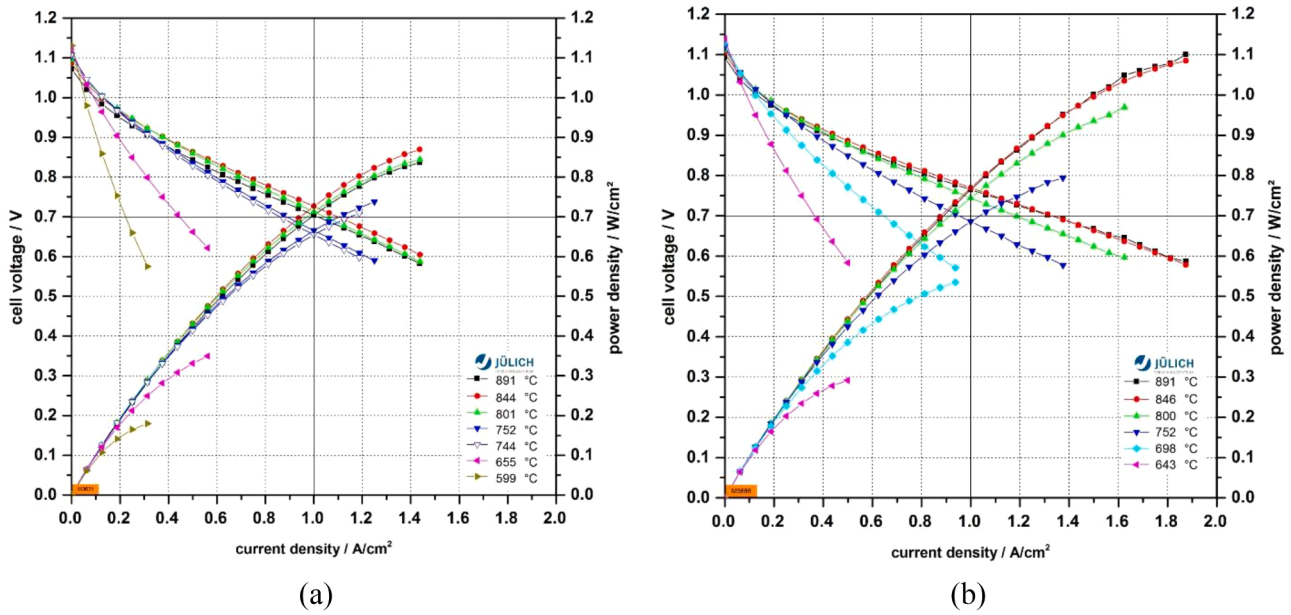

Fig. 10. Voltammetric characteristics of single button SOFCs with LSFC (a) and $Pr_2NiO_{4+\delta}$ (b) cathodes [40].

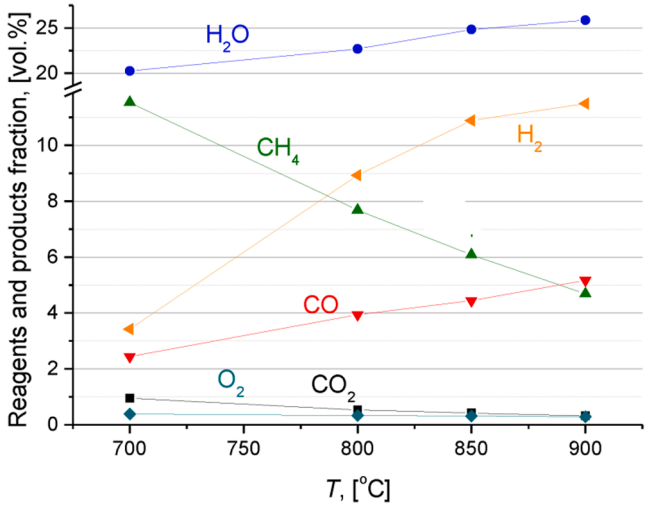

Fig. 11. CH_4 partial oxidation in the catalytic membrane reactor (feed: 10% CH_4 in He at 3.6 l/h, air at 1.5 l/h).

with oxygen transport characteristics in the electrode material (tracer diffusion coefficient, surface exchange constant) was revealed (Fig. 9). The electrochemical properties of the symmetric cells studied were found to be inversely proportional to the product of the oxygen tracer diffusion coefficient and surface exchange constant which agrees with the theoretical model of the relationship between the diffusion impedance and kinetic parameters of the electrode materials (Adler – Lane – Steele model) [8,9,14].

According to the results of testing single-button solid oxide fuel cells with cathodes fabricated from $Pr_2NiO_{4+\delta}$ and PNC – YDC, the maximum power density was ~ 0.3 W/cm^2 and ~ 0.5 W/cm^2 at 600 °C and 700 °C, respectively [5,11,14,39,40]. These characteristics were reached due to the high oxygen mobility and surface reactivity of these materials as well as their high electronic conductivity. The maximum power density values obtained for SOFCs with $Pr_2NiO_{4+\delta}$ and PNC – YDC cathodes are comparable to, or even higher than those for the cells with LSM and LSFC cathodes deposited on the same anode half-cells (Fig. 10) [5,7,11,14,39,40].

4.4. Performance of asymmetric supported membranes for oxygen separation

According to the tests of membranes with the PNC – YDC functional layers in methane partial oxidation and oxi-dry reforming, no significant carbonization of the membrane surface was observed. Syngas selectivity in the methane partial oxidation increases with the increase of methane concentration in the inlet gas mixture and temperature (Fig. 11). For the high feed rates, an increase of the syngas yield and a decrease in carbon dioxide content were revealed. These performance characteristics are the result of a high oxygen permeation flux (up to ~ 7–10 ml O_2/(cm^{2}min) at 950 °C) caused by the high oxygen mobility of the PNC – YDC nanocomposite [5,14,41,42].

5. Conclusions

Studies of oxygen mobility and the surface reactivity of RP phases and perovskite-fluorite nanocomposites as novel materials for the oxygen separation membranes' permselective layers and SOFC cathodes from the perspective of their structural and textural features, were reviewed. The role of the cooperative oxygen migration mechanism, cation redistribution features and developed interfaces in nanocomposites in enhancing the oxygen mobility was highlighted. The superior performance characteristics of the SOFC cathodes and oxygen separation membranes were shown to derive from fast oxygen transport along with optimized composition and nanodomain structure as well as high electric conductivity and chemical stability.

CRediT authorship contribution statement

Vladislav A. Sadykov: Conceptualization, Writing - review & editing, Supervision. **Ekaterina M. Sadovskaya:** Formal analysis. **Nikita F. Eremeev:** Investigation, Formal analysis. **Elena Yu. Pikalova:** Investigation. **Nina M. Bogdanovich:** Investigation. **Elena A. Filonova:** Investigation. **Tamara A. Krieger:** Investigation, Formal analysis. **Yulia E. Fedorova:** Investigation. **Alexey V. Krasnov:** Investigation. **Pavel I. Skriabin:** Investigation. **Anton I. Lukashevich:** Investigation. **Robert Steinberger-Wilckens:** Investigation. **Izaak C. Vinke:** Investigation.

Declaration of Competing Interest

The authors declare that they have no known competing financial interests or personal relationships that could have appeared to influence the work reported in this paper.

Acknowledgements

Support of different parts of the work by the Russian Science Foundation (Project 16-13-00112) and the budget project #AAAA-A17-117041110045-9 for Boreskov Institute of Catalysis is gratefully acknowledged. The authors from the Ural Federal University are grateful to the Government of the Russian Federation (Agreement 02.A03.21.0006, Act 211). $Ce_{0.9}Y_{0.1}O_{2-\delta}|Ce_{0.9}Gd_{0.1}O_{2-\delta}|Ni/Zr_{0.84}Y_{0.16}O_{2-\delta}$ anodic half-cells and Ni/Al foam substrates were kindly provided by H. C. Starck, Germany and Powder Metallurgy Institute NAN Belarus, respectively. Authors would like to appreciate International Conference on Advances in Energy Systems and Environmental Engineering (ASEE19, Wroclaw, Poland, June 9-12, 2019) Organization Committee.

References

[1] B.C.H. Steele, A. Heinzel, Materials for fuel-cell technologies, in Materials for Sustainable Energy, World Scientific Publishing Co Pte Ltd, Co-Published with Macmillan Publishers Ltd, UK, 2010.
[2] R.N. Basu, Materials for solid oxide fuel cells, in Recent Trends in Fuel Cell Science and Technology, Springer, New York, 2007.
[3] R.M. Ormerod, Solid oxide fuel cells, Chem. Soc. Rev. 32 (2003) 17–28.
[4] V.A. Sadykov, S.N. Pavlova, T.S. Kharlamova, V.S. Muzykantov, N.F. Uvarov, Y.S. Okhlupin, A.V. Ishchenko, A.V. Bobin, N.V. Mezentseva, G.M. Alikina, A.I. Lukashevich, T.A. Krieger, T.V. Larina, N.N. Bulgakov, V. M. Tapilin, V.D. Belyaev, E.M. Sadovskaya, A.I. Boronin, V.A. Sobyanin, O.F. Bobrenok, A.L. Smirnova, O.L. Smorygo, J.A. Kilner,, Perovskites and their nanocomposites with fluorite-like oxides as materials for solid oxide fuel cells cathodes and oxygen-conducting membranes: Mobility and reactivity of the surface/bulk oxygen as a key factor of their performance, in: Perovskites: Structure, Properties and Uses, Nova Science Publishers, New York, 2010, pp. 67–168.
[5] V.A. Sadykov, N.V. Mezentseva, L.N. Bobrova, O.L. Smorygo, N.F. Eremeev, Y. E. Fedorova, Y.N. Bespalko, P.I. Skriabin, A.V. Krasnov, A.I. Lukashevich, T. A. Krieger, E.M. Sadovskaya, V.D. Belyaev, A.N. Shmakov, Z.S. Vinokurov, V. A. Bolotov, Y.Y. Tanashev, M.V. Korobeynikov, M.A. Mikhailenko, in: Advanced materials for solid oxide fuel cells and membrane catalytic reactors, Elsevier, Advanced Nanomaterials for Catalysis and Energy, 2019, pp. 435–514.
[6] V.A. Sadykov, E.M. Sadovskaya, N.F. Eremeev, P.I. Skriabin, A.V. Krasnov, Y. N. Bespalko, S.N. Pavlova, Y.E. Fedorova, E.Y. Pikalova, A.V. Shlyakhtina, Oxygen mobility in the materials for solid oxide fuel cells and catalytic membranes (review), Russ. J. Electrochem. 55 (2019) 701–718.
[7] V.A. Sadykov, V.S. Muzykantov, N.F. Yeremeev, V.P. Pelipenko, E.M. Sadovskaya, A.S. Bobin, Y.E. Fedorova, D.G. Amanbaeva, A.L. Smirnova, Solid oxide fuel cell cathodes: Importance of chemical composition and morphology, Catal. Sust. Energ. 2 (2015) 57–70.
[8] S.B. Adler, Factors governing oxygen reduction in solid oxide fuel cell cathodes, Chem. Rev. 104 (2004) 4791–4844.
[9] S.B. Adler, J.A. Lane, B.C.H. Steele, Electrode kinetics of porous mixed-conducting oxygen electrodes, J. Electrochem. Soc. 143 (1996) 3554–3564.
[10] E. Boehm, J.M. Bassat, P. Dordor, F. Mauvy, J.C. Grenier, P. Stevens, Oxygen diffusion and transport properties in non-stoichiometric $Ln_{2-x}NiO_{4+\delta}$ oxides, Solid State Ionics 176 (2005) 2717–2725.
[11] R.D. Shannon, Revised effective ionic radii and systematic studies of interatomic distances in halides and chalcogenides, Acta Crystallographica Section A: Crystal Phys. Diffr. Theoretical General Crystallogr. 32 (1976) 751–767.
[12] V.A. Sadykov, N.F. Eremeev, E.M. Sadovskaya, A.S. Bobin, Y.E. Fedorova, V. S. Muzykantov, N.V. Mezentseva, G.M. Alikina, T.A. Kriger, V.D. Belyaev, V. A. Rogov, A.S. Ulikhin, Y.S. Okhlupin, N.F. Uvarov, O.F. Bobrenok, N. McDonald, J. Watton, A. Dhir, R. Steinberger-Wilckens, J. Mertens, I.C. Vinke, Cathodic materials for intermediate-temperature solid oxide fuel cells based on praseodymium nickelates-cobaltites, Russ. J. Electrochem. 50 (2014) 669–679.
[13] V. Sadykov, N. Eremeev, G. Alikina, E. Sadovskaya, V. Muzykantov, V. Pelipenko, A. Bobin, T. Krieger, V. Belyaev, V. Ivanov, A. Ishchenko, V. Rogov, A. Ulihin, N. Uvarov, Y.u. Okhlupin, J. Mertens, I. Vinke, Oxygen mobility and surface reactivity of $PrNi_{1-x}Co_xO_{3+\delta}$–$Ce_{0.9}Y_{0.1}O_{2-\delta}$ cathode nanocomposites, Solid State Ionics 262 (2014) 707–712.
[14] V.A. Sadykov, N.F. Eremeev, Z.S. Vinokurov, A.N. Shmakov, V.V. Kriventsov, A. I. Lukashevich, A.V. Krasnov, A.V. Ishchenko, Structural studies of Pr nickelate-cobaltite – Y-doped ceria nanocomposite, J. Ceram. Sci. Technol. 8 (2017) 129–140.
[15] V. Sadykov, E. Sadovskaya, N. Eremeev, E. Pikalova, N. Bogdanovich, E. Filonova, Y.u. Fedorova, A. Krasnov, P. Skriabin, A. Lukashevich, Design of materials for solid oxide fuel cells cathodes and oxygen separation membranes based on fundamental studies of their oxygen mobility and surface reactivity, E3S Web Conf 116 (2019) 00068.
[16] C. Ferchaud, J.-C. Grenier, Y. Zhang-Steenwinkel, M.M.A. van Tuel, F.P.F. van Berkel, J.-M. Bassat, High performance praseodymium nickelate oxide cathode for low temperature solid oxide fuel cell, J. Power Sources 196 (2011) 1872–1879.
[17] X.-D. Zhou, J.W. Templeton, Z. Nie, H. Chen, J.W. Stevenson, L.R. Pederson, Electrochemical performance and stability of the cathode for solid oxide fuel cells: V. high performance and stable Pr_2NiO_4 as the cathode for solid oxide fuel cells, Electrochim. Acta 71 (2012) 44–49.
[18] X. Meng, S. Lü, S. Liu, X. Liu, Y. Sui, X. Li, M. Pang, B. Wang, Y. Ji, M.Z. Hu, Electrochemical characterization of B-site cation-excess $Pr_2Ni_{0.75}Cu_{0.25}Ga_{0.05}O_{4+\delta}$ cathode for IT-SOFCs, Ceram. Int. 41 (2015) 12107–12114.
[19] G. Amow, I.J. Davidson, S.J. Skinner, A comparative study of the Ruddlesden-Popper series, $La_{n+1}Ni_nO_{3n+1}$ (n= 1, 2 and 3), for solid-oxide fuel-cell cathode applications, Solid State Ionics 177 (2006) 1205–1210.
[20] P.-M. Geffroy, M. Reichmann, T. Chartier, J.-M. Bassat, J.-C. Grenier, Evaluating oxygen diffusion, surface exchange and oxygen semi-permeation in $Ln_2NiO_{4+\delta}$ membranes (Ln= La, Pr and Nd), J. Memb. Sci. 451 (2014) 234–242.
[21] T. Ishihara, S. Miyoshi, T. Furuno, O. Sanguanruang, H. Matsumoto, Mixed conductivity and oxygen permeability of doped Pr_2NiO_4-based oxide, Solid State Ionics 177 (2006) 3087–3091.
[22] T. Ishihara, N. Sirikanda, K. Nakashima, S. Miyoshi, H. Matsumoto, Mixed oxide ion and hole conductivity in $Pr_{2-\alpha}Ni_{0.76-x}Cu_{0.24}Ga_xO_{4+\delta}$ membrane, J. Electrochem. Soc. 157 (2010) B141–B146.
[23] S. Miyoshi, T. Furuno, O. Sanguanruang, H. Matsumoto, T. Ishihara, Mixed conductivity and oxygen permeability of doped Pr_2NiO_4-based oxides, J. Electrochem. Soc. 157 (1) (2010) B57–B62.
[24] X. Li, N.A. Benedek, Enhancement of ionic transport in complex oxides through soft lattice modes and epitaxial strain, Chem. Mater. 27 (2015) 2647–2652.
[25] L. Minervini, R.W. Grimes, J.A. Kilner, K.E. Sickafus, Oxygen migration in $La_2NiO_{4+\delta}$, J. Mater. Chem. 10 (2000) 2349–2354.
[26] A. Kushima, D. Parfitt, A. Chroneos, B. Yildiz, J.A. Kilner, R.W. Grimes, Interstitialcy diffusion of oxygen in tetragonal $La_2CoO_{4+\delta}$, Phys. Chem. Chem. Phys. 13 (2011) 2242–2249.
[27] V.A. Sadykov, E.M. Sadovskaya, E.Y. Pikalova, A.A. Kolchugin, E.A. Filonova, S. M. Pikalov, N.F. Eremeev, A.V. Ishchenko, A.I. Lukashevich, J.M. Bassat, Transport features in layered nickelates: correlation between structure, oxygen diffusion, electrical and electrochemical properties, Ionics 24 (2018) 1181–1193.
[28] V.A. Sadykov, E.Y. Pikalova, A.A. Kolchugin, E.A. Filonova, E.M. Sadovskaya, N. F. Eremeev, A.V. Ishchenko, A.V. Fetisov, S.M. Pikalov, Oxygen Transport properties of Ca-doped Pr_2NiO_4, Solid State Ionics 317 (2018) 234–243.
[29] E.Y. Pikalova, A.A. Kolchugin, V.A. Sadykov, E.M. Sadovskaya, E.A. Filonova, N. F. Eremeev, N.M. Bogdanovich, Structure, transport properties and electrochemical behavior of the layered lanthanide nickelates doped with calcium, Int. J. Hydrogen Energy 43 (2018) 17373–17386.
[30] V.A. Sadykov, E.Y. Pikalova, Z.S. Vinokurov, A.N. Shmakov, N.F. Eremeev, E. M. Sadovskaya, J.G. Lyagaeva, D.A. Medvedev, V.D. Belyaev, Tailoring the structural, thermal and transport properties of $Pr_2NiO_{4+\delta}$ through Ca-doping strategy, Solid State Ionics 333 (2019) 30–37.
[31] E.Y. Pikalova, V.A. Sadykov, E.A. Filonova, N.F. Eremeev, E.M. Sadovskaya, S. M. Pikalov, N.M. Bogdanovich, J.G. Lyagaeva, A.A. Kolchugin, L.B. Vedmid', A. V. Ishchenko, V.B. Goncharov, Structure, oxygen transport properties and electrode performance of Ca-substituted Nd_2NiO_4, Solid State Ionics 335 (2019) 53–60.
[32] V.A. Sadykov, E.Y. Pikalova, A.A. Kolchugin, A.V. Fetisov, E.M. Sadovskaya, E. A. Filonova, N.F. Eremeev, V.B. Goncharov, A.V. Krasnov, P.I. Skriabin, A. N. Shmakov, Z.S. Vinokurov, A.V. Ishchenko, S.M. Pikalov, Transport properties of Ca-doped Ln_2NiO_4 for intermediate temperature solid oxide fuel cells cathodes and catalytic membranes for hydrogen production, Int. J. Hydrogen Energy 45 (2020) 13625–13642.
[33] V.A. Sadykov, N.F. Eremeev, V.V. Usol'tsev, A.S. Bobin, G.M. Alikina, V. V. Pelipenko, E.M. Sadovskaya, V.S. Muzykantov, N.N. Bulgakov, N.F. Uvarov, Mechanism of oxygen transfer in layered lanthanide nickelates $Ln_{2-x}NiO_{4+\delta}$ (Ln = La, Pr) and their nanocomposites with $Ce_{0.9}Gd_{0.1}O_{2-\delta}$ and $Y_2(Ti_{0.8}Zr_{0.2})_{1.6}Mn_{0.4}O_{7-\delta}$ solid electrolytes, Russ. J. Electrochem. 49 (2013) 645–651.
[34] A.A. Kolchugin, E.Y. Pikalova, N.M. Bogdanovich, D.I. Bronin, S.M. Pikalov, S. V. Plaksin, M.V. Ananyev, V.A. Eremin, Structural, electrical and electrochemical properties of calcium-doped lanthanum nickelate, Solid State Ionics 288 (2016) 48–53.
[35] FullProf Suite, Crystallographic tools for Rietveld, profile matching and integratedintensity refinements of X-ray and/or neutron data, Available at https://www.ill.eu/sites/fullprof/.
[36] V.A. Sadykov, E.M. Sadovskaya, N.F. Uvarov, Methods of isotopic relaxations for estimation of oxygen diffusion coefficients in solid electrolytes and materials with mixed ionic-electronic conductivity, Russ. J. Electrochem. 51 (2015) 458–467.
[37] V. Sadykov, E. Sadovskaya, A. Bobin, T. Kharlamova, N. Uvarov, A. Ulikhin, C. Argirusis, G. Sourkouni, V. Stathopoulos, Temperature-programmed $C^{18}O_2$ SSITKA for powders of fast oxide-ion conductors: Estimation of oxygen self-diffusion coefficients, Solid State Ionics 271 (2015) 69–72.
[38] E.M. Sadovskaya, V.V. Skazka, A.S. Bobin, Isotopic transient analysis of oxygen exchange over oxides, Chem. Eng. J. 348 (2018) 1025–1036.
[39] E.Y. Pikalova, N.M. Bogdanovich, A.A. Kolchugin, D.A. Osinkin, D.I. Bronin, Electrical and electrochemical properties of $La_2NiO_{4+\delta}$-based cathodes in contact with $Ce_{0.8}Sm_{0.2}O_{2-\delta}$ electrolyte, Procedia Eng. 98 (2014) 105–110.

[40] V. Sadykov, N. Eremeev, E. Sadovskaya, A. Bobin, A. Ishchenko, V. Pelipenko, Y. Fedorova, A. Lukashevich, A. Salanov, T. Krieger, V. Belyaev, V. Rogov, V. Muzykantov, Z. Vinokurov, A. Shmakov, O. Bobrenok, N. Uvarov, Y. Ohlupin, A. Ulikhin, J. Mertens, I.C. Vinke, R. Steinberger-Wilckens, J. Watton, A. Dhir, N. McDonalds, IT SOFC cathodes based on Pr nickelates/cobaltites: design and performance, in, in: Proceedings of the 11th European SOFC and SOE, 2014, pp. 20–28.
[41] V.A. Sadykov, Yu.E. Fedorova, A.I. Lukashevich, Z.Y. Vostrikov, N.F. Eremeev, A. V. Krasnov, P.I. Skryabin, O.L. Smorygo, Novel nanocomposite materials based on praseodymium nickelate-cobaltite for oxygen separation membranes, Mat. Today Proc. 4 (2017) 11351–11355.
[42] V.A. Sadykov, A.V. Krasnov, Y.E. Fedorova, A.I. Lukashevich, Y.N. Bespalko, N. F. Eremeev, P.I. Skriabin, K.R. Valeev, O.L. Smorygo, Novel nanocomposite materials for oxygen and hydrogen separation membranes, Int. J. Hydrogen Energy 45 (2020) 13575–13585.
[43] V.S. Muzykantov, V.V. Popovskii, G.K. Boreskov, Kinetics of isotope exchange in a molecular oxygen–solid oxide system, Kin. Cat. (in Russian) 5 (1964) 624–629.
[44] V.S. Muzykantov, E. Kemnitz, V.A. Sadykov, V.V. Lunin, Interpretation of isotope exchange data "without time": Nonisothermal exchange of dioxygen with oxides, Kin. Cat. 44 (2003) 319–322.
[45] V.S. Muzykantov, Studies of dioxygen activation on oxide catalysts for oxidation: Problems, results and perspectives, React. Kinet. Catal. Lett. 35 (1987) 437–447.
[46] V.A. Sadykov, E.M. Sadovskaya, V.V. Skazka, N.F. Eremeev, P.I. Skriabin, A. V. Krasnov, Yu.N. Bespalko, S.N. Pavlova, Yu.E. Fedorova, E.Yu. Pikalova, A. V. Shlyakhtina, Isothermal and temperature-programmed isotope exchange of oxygen in a flow reactor for SOFC and catalytic membranes materials, in: ISOTOPCAT 2019 (International Symposium "Isotopic Studies in Catalysis and Electrocatalysis) July 3–5, Poitiers, France, 2019, pp. 25–26.
[47] S. Xu, R. Jacobs, D. Morgan, Factors controlling oxygen interstitial diffusion in the Ruddlesden-Popper oxide $La_{2-x}Sr_xNiO_{4+\delta}$, Chem. Mater. 30 (2018) 7166–7177.
[48] D. Lee, H.N. Lee, Controlling oxygen mobility in Ruddlesden-Popper oxides, Materials 10 (2017) 368.
[49] C. Tealdi, C. Ferrara, P. Mustarelli, M.S. Islam, Vacancy and interstitial oxide ion migration in heavily doped $La_{2-x}Sr_xCoO_{4\pm\delta}$, J. Mater. Chem. 22 (2012) 8969–8975.
[50] R.P. Forslund, W.G. Hardin, X. Rong, A.M. Abakumov, D. Filimonov, C. T. Alexander, J.T. Mefford, H. Iyer, A.M. Kolpak, K.P. Johnston, K.J. Stevenson, Exceptional electrocatalytic oxygen evolution via tunable charge transfer interactions in $La_{0.5}Sr_{1.5}Ni_{1-x}Fe_xO_{4\pm\delta}$ Ruddlesden-Popper oxides, Nat. Commun. 9 (2018) 3150.
[51] T.L. Meyer, R. Jacobs, D. Lee, L. Jiang, J.W. Freeland, C. Sohn, H.N. Lee, Strain control of oxygen kinetics in the Ruddlesden-Popper oxide $La_{1.85}Sr_{0.15}CuO_4$, Nat. Commun. 9 (2018) 92.
[52] V.A. Sadykov, S.N. Pavlova, Z.S. Vinokurov, A.N. Shmakov, N.F. Eremeev, Y. E. Fedorova, E.P. Yakimchuk, V.V. Kriventsov, V.A. Bolotov, Y.Y. Tanashev, E. M. Sadovskaya, S.V. Cherepanova, K.V. Zolotarev, Application of SR methods for the study of nanocomposite materials for hydrogen energy, Phys. Procedia 84 (2016) 397–406.
[53] V. Sadykov, N. Eremeev, E. Sadovskaya, A. Bobin, A. Ishchenko, V. Pelipenko, V. Muzykantov, T. Krieger, D. Amanbaeva, Oxygen mobility and surface reactivity of $PrNi_{1-x}Co_xO_{3-\delta}$ perovskites and their nanocomposites with $Ce_{0.9}Y_{0.1}O_{2-\delta}$ by temperature-programmed isotope exchange experiments, Solid State Ionics 273 (2015) 35–40.
[54] M.Yu. Sinev, G.W. Graham, L.P. Haack, M. Shelef, Kinetic and structural studies of oxygen availability of the mixed oxides $Pr_{1-x}M_xO_y$ (M = Ce, Zr), J. Mater. Res. 11 (1996) 1960–1971.
[55] K. Ahn, D.S. Yoo, D.H. Prasad, H.-W. Lee, Y.-Ch. Chung, J.-H. Lee, Role of multivalent Pr in the formation and migration of oxygen vacancy in Pr-doped ceria: experimental and first-principles investigations, Chem. Mater. 24 (2012) 4261–4267.
[56] G.E. Murch, The Nernst-Einstein equation in high-defect content solids, Philos, Mag, A 45 (1982) 685–692.
[57] H. Takamura, J. Kobayashi, N. Takahashi, M. Okada, Electrical conductivity of ceria nanoparticles under high pressure, J. Electroceram. 22 (2009) 24–32.
[58] X. Qi, Y.S. Lin, C.T. Holt, S.L. Swartz, Electric conductivity and oxygen permeability of modified cerium oxides, J. Mater. Sci. 38 (2003) 1073–1079.
[59] V. Sadykov, N. Mezentseva, M. Arapova, T. Krieger, E. Gerasimov, G. Alikina, V. Pelipenko, A. Bobin, V. Muzykantov, Y. Fedorova, E. Sadovskaya, N. Eremeev, V. Belyaev, Y. Okhlupin, N. Uvarov, Fast oxygen transport in bismuth oxide containing nanocomposites, Solid State Ionics 251 (2013) 34–39.
[60] M. Burriel, J. Pena-Martinez, R.J. Chater, S. Fearn, A.V. Berenov, S.J. Skinner, J. A. Kilner, Anisotropic oxygen ion diffusion in layered $PrBaCo_2O_{5+\delta}$, Chem. Mater. 24 (3) (2012) 613–621.
[61] G. Kim, S. Wang, A.J. Jacobson, L. Reimus, P. Brodersen, C.A. Mims, Rapid oxygen ion diffusion and surface exchange kinetics in $PrBaCo_2O_{5+x}$ with a perovskite related structure and ordered A cations, J. Mater. Chem. 17 (2007) 2500–2505.